Applied Surface Science 531 (2020) 147415

Contents lists available at ScienceDirect

Applied Surface Science

journal homepage: www.elsevier.com/locate/apsusc

Ultrasonication–dry-based synthesis of gold nanoparticle-supported CuFe on rGO nanosheets for competent detection of biological molecules

Vijayakumar Elayappan[a], Selvaganapathy Muthusamy[b], Gopiraman Mayakrishnan[c], Ramkumar Balasubramaniam[d], Yun-Sung Lee[d], Hyun Sung Noh[a], Dawool Kwon[a], Mtangi Mohamed Mussa[a], Haigun Lee[a,*]

[a] Department of Materials Science and Engineering, Korea University, Seoul 02841, Republic of Korea
[b] Department of Chemistry, ACS College of Engineering, Bengaluru, Karnataka 560074, India
[c] Department of Applied Bioscience, College of Life & Environment Science, Konkuk University, 120 Neungdong-ro, Gwangjin-gu, Seoul 05029, Republic of Korea
[d] Faculty of Applied Chemical Engineering, Chonnam National University, Gwangju 500 757, Republic of Korea

ARTICLE INFO

Keywords:
Ultrasonication
Dry synthesis
Sensor
Copper ferrite
rGO

ABSTRACT

This study details the synthesis of gold (Au) nanoparticle-supported copper ferrite (CF) over reduced graphene oxide (Au-CF@rGO) through ultrasonication–dry synthesis techniques. The vigorous stormy mixing and acoustic cavitation acquired from the intense shock waves produced during ultrasonication can effectively irradiate the reaction conditions. The as-synthesized nanoparticles exhibit excellent crystallinity as well as homogeneous distribution over rGO nanosheets, as established by XRD, HR-TEM, Raman, XPS, and EDX analysis. Furthermore, the electrochemical analysis by cyclic voltammetry and differential pulse voltammetry (DPV) technique was accomplished by fabricating an Au-CF@rGO/GCE modified electrode. Interestingly, the DPV studies of the modified Au-CF@rGO/GCE electrode detects the dopamine (DA) in the linear concentration ranges from 0.001 to 119.6 μM, a low detection limit of 0.001 μM, a limit of detection of 0.34 nM, and enhanced sensitivity of 8.743 $\mu A \mu M^{-1} cm^{-2}$. The excellent electrochemical property towards the detection of DA indicates the successful formation of strongly anchored Au-CF nanoparticles on rGO nanosheets. Conversely, the modified Au-CF@rGO/GCE electrode shows excellent reproducibility, repeatability, and selectivity with excellent storage stability. In addition, the electrochemical sensor was used to examine real samples to determine the amount of DA present in commercially available banana milk samples, with a sensing efficiency of approximately 99%.

1. Introduction

The human central nervous system neurotransmitter of dopamine (DA) plays several roles in the function of physiological activities, including stress, motivated behaviors, reward-driven learning, memory, mood, and mental cognition. Therefore, the imbalance of DA concentrations in human blood and brain systems may reason for neurological syndromes such as Parkinson's disease, Alzheimer's disease, Schizophrenia, depression, addiction, and Tourette's syndrome [1–10]. Therefore, the quantitative and sensitive detection of DA for observing its levels in the human body is necessary. So far, numerous qualitative and quantitative approaches have been employed to examine DA levels in the human body such as calorimetry, spectrophotometry, fluorescence, chemiluminescence, capillary electrophoresis, and micro-dialysis [11–19]. However, the aforementioned techniques suffer drawbacks, including long analysis time, expensive reagents, lack of selectivity, and expensive instrumentation. In addition, extracellular DA levels in the cerebrum vary on a subsecond time scale fluctuate on a sub-second timescale because of the phasic firing of DA neurons. Moreover, accurate measurements at short timescales and detection at low concentration levels are essential yet challenging, impeding the practical application of many techniques.

Therefore, a fast and cost-effective technique with high accuracy for low concentration of DA is highly desirable. Electrochemical sensing techniques can offer monitoring for the fast chemical changes that result from discrete neurochemical actions with fast sampling rates from the micro to millisecond time scale [20]. However, conventional electrochemical techniques are insufficient for the detection of DA at nanomolar levels. To overcome these problems, the determination of DA by chemically modified electrocatalysts coupled with the use of catalytically active nanomaterials has attained due to its great sensitivity, resistance to surface fouling, effective mass transport, excellent

* Corresponding author.
E-mail address: haigunlee@korea.ac.kr (H. Lee).

https://doi.org/10.1016/j.apsusc.2020.147415
Received 26 June 2020; Received in revised form 25 July 2020; Accepted 29 July 2020
Available online 01 August 2020
0169-4332/

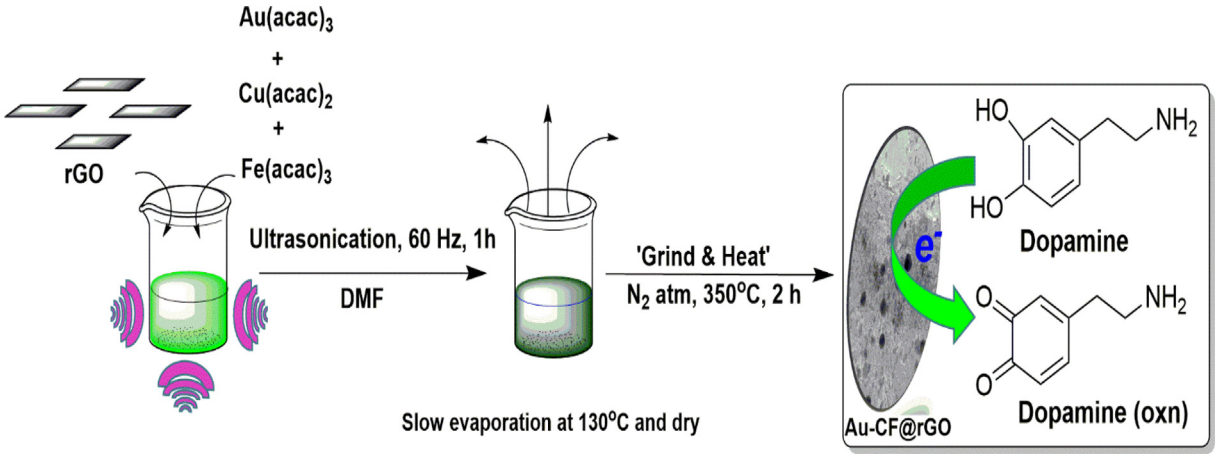

Scheme 1. US–DS route for the preparation of the Au-CF@rGO nanostructured material.

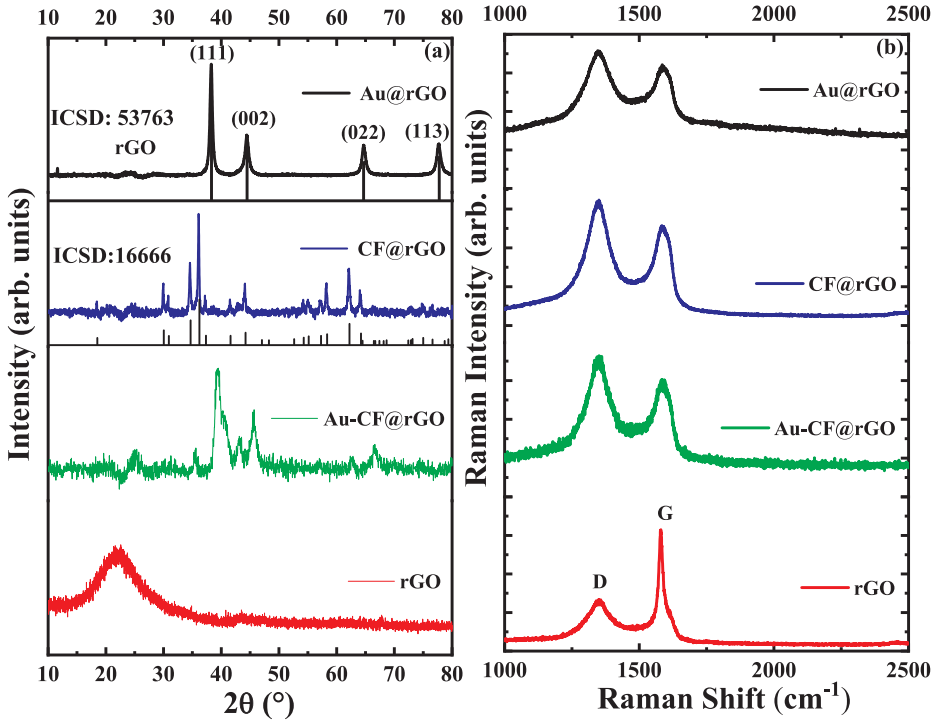

Fig. 1. (a) XRD and (b) Raman analysis of the rGO, Au-CF@rGO, CF@rGO, and Au@rGO nanomaterials.

stability, and better controllability in local micro environment. Transition metals, transition metal oxides, noble metal nanoparticles, and carbon-based nanostructured materials have been reported as effective electrocatalysts for the detection of DA in low concentrations because they possess various physical and chemical properties [4,7,10,21]. Among them, some bimetallic transition metal oxides (ABO_x, where A and B stands for transition metals) deserve significant attention owing to their prominent electrocatalytic activities, stability, high natural abundance, and low cost. In particular, copper-based electrocatalysts have been widely studied because of their superior electrocatalytic performances in numerous electrochemical energy devices related applications, such as biosensors, drug sample analyzers, solar cells, batteries, and water splitters, among others [22–26]. Recently, Achary et al. [27] reported that spinel copper ferrite ($CuFe_2O_4$) exhibits an increased magnitude of electrocatalytic performance because of its magnetic and dielectric properties, and it offers specific properties such as moisture insensitivity, high reactivity, and environmentally benign nature. However, the low sensitivity and selectivity of $CuFe_2O_4$ are major concerns deterring its use for sensing applications. These limitations can be overcome by the hybridization of spinel $CuFe_2O_4$ with suitable carbon-based support material. Thus, the hybridization of $CuFe_2O_4$ and rGO offers a promising solution to improve electron transport and boost the electrocatalytic activity of $CuFe_2O_4$. Among the various carbon nanostructured materials, reduced graphene oxide (rGO) possesses the best attractive properties, including high thermal stability, higher specific surface area, great electrical and thermal conductivity, high carrier mobility, and greater mechanical properties, among others. In addition, the oxygenated functional groups present in rGO sheets allow them to accept a wide range of mono-, bi-, and trimetallic nanoparticles through covalent or non-covalent interactions [28–32]. Further, to increase the sensitivity of $CuFe_2O_4$@rGO, gold nanoparticles were decorated over the synthesized $CuFe_2O_4$@rGO, because they can provide more rapid and higher sensing current responses during electrochemical sensing applications [33,34]. Preparation technique also requires further attention for effectively fabricating sensing electrodes. Numerous techniques are used to prepare hybrid

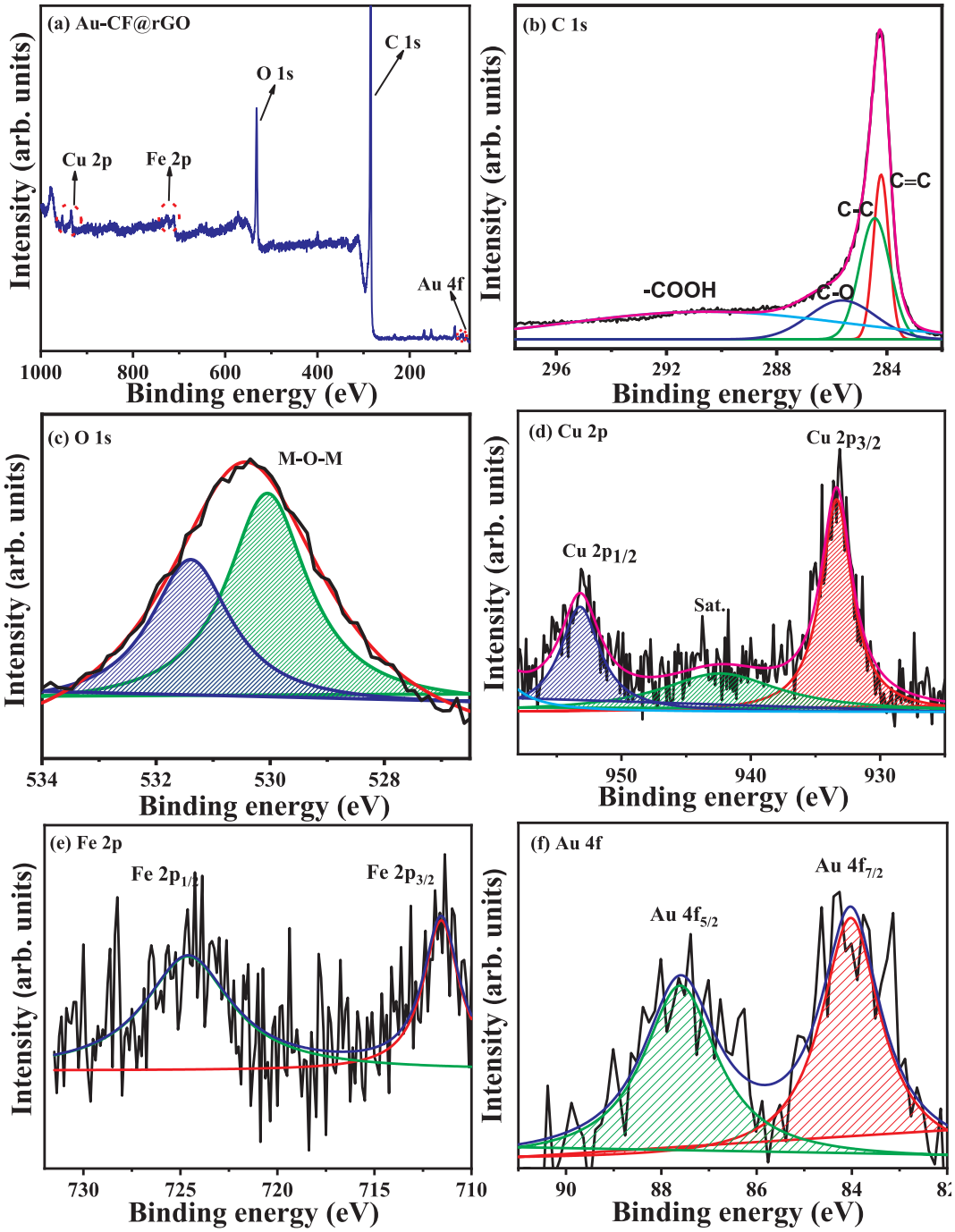

Fig.2. (a) XPS spectra survey of Au-CF@rGO and the corresponding deconvoluted spectra of the (b) C 1s, (c) O 1s, (d) Cu 2p, (e) Fe 2p, and (f) Au 4f regions.

nanostructured materials, such as hydrothermal, precipitation, sol–gel, and solvothermal synthesis routes. Usually, the chemical and physical properties of the nanostructured materials are significantly determined by the preparation techniques used. In the last few years, ultrasonic-assisted nanostructured material synthesis has garnered great interest owing to its reputation as a green, economical, and rapid synthetic tool and ability to produce narrow size distributions under mild conditions [35–43]. Moreover, the nanostructured materials prepared through ultrasonication–dry synthesis (US–DS) exhibit high phase purity, defined surface morphology, extensive defect sites, large surface-active areas, and highly crystalline nanoparticles that are strongly and homogeneously attached to each layer of the conductive rGO matrix.

Given these facts, this study presents the development of a highly selective and stable DA sensing electrode material consisting of gold-supported copper-ferrite on an rGO nanostructure synthesized by an US–DS method. The physical and electrochemical properties of the prepared gold (Au) nanoparticle-decorated $CuFe_2O_4$@rGO (Au-CF@rGO) are investigated and compared with $CuFe_2O_4$@rGO (CF@rGO) and Au@rGO. The fabricated Au-CF@rGO/GCE (modified electrode) glassy carbon electrode exhibits excellent sensing properties, such as a broad linear range of 0.001–119.6 μM, a limit of detection (LOD) of 0.34 nM, a lower detection limit of 0.001 μM, and enhanced sensitivity of 8.743 $\mu A \mu M cm^{-2}$ for DA.

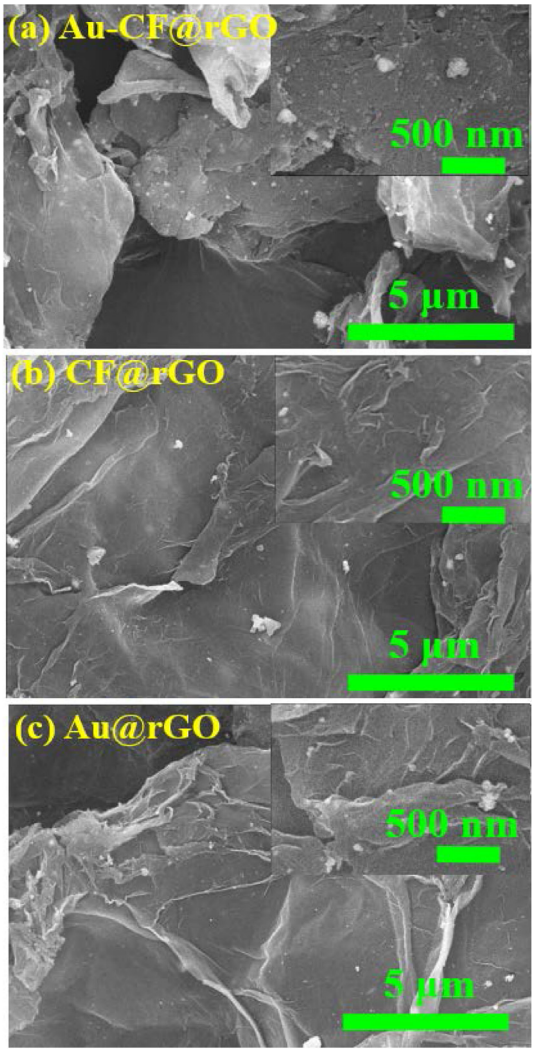

Fig. 3. FEM-SEM images of (a) Au-CF@rGO, (b) CF@rGO, and (c) Au@rGO.

2. Experimental section

2.1. Materials

ACS materials; rGO (purity > 99 wt%). Sigma Aldrich; gold acetate ($Au(acac)_3$) (97%), iron acetate ($Fe(acac)_3$), copper acetate ($Cu(acac)_2$), dimethylformamide (DMF), phosphate buffer solution (PBS). All materials procured in this experiment were used as received.

2.2. Synthesis of Au-CF@rGO, Au@rGO, and CF@rGO

Au-CF@rGO, Au@rGO, and CF@rGO electrode materials were synthesized by the US–DS method. Formation of high-intensity shock-waves during ultrasonic irradiation in aqueous solution induces acoustic cavitation, which aids in concentrating the dispersed sound energy. This acoustic cavitation can generate heat energy up to 5000 K and pressures of 500 atm with a cooling rate of 1010 Ks^{-1}. The high levels of energy generated during these turbulent conditions are extremely useful to nanostructured chemical synthesis [44–46]. Because of these properties, ultrasonic waves have become a favored reaction technique for the efficient synthesis of nanostructured materials. A dry synthesis method was performed as a follow-up to greatly enhance the number of defect sites in the rGO nanosheets, which help to create higher number of active sensing sites. Furthermore, mono-, bi-, and tri-metallic nanomaterials are easily anchored inside these nanostructures, providing more electrochemically active sites with excellent conductivity [47,48]. The notable benefits of the US–DS method are the effective formation of homogeneously dispersed nanoparticles that create more active sites, improve the conductivity, and excellent stability during electrochemical studies.

DMF was used in this synthesis techniques mainly to obtain the homogeneous dispersion of the metal salts on carbon nanostructures and provide excellent nanoparticle morphology [47]. Moreover, the acac ligands are decomposed at high temperatures (calcinations process) to form nanoparticles on carbon nanostructures. Here, during the decomposition process, the acac ligand assists for better adhesion of nanoparticles to the support carbon nanostructures during the decomposition process. During the calcinations process, the acac ligands typically act as bridge between nanoparticles and carbon support, thus, better adhesion of nanoparticles with carbon nanostructure support achieved [49]. This homogeneous solution of precursors was ultrasonicated for 1 h and then allow to slow evaporated at 100 °C until a condensed paste formed.

In a typical synthesis of Au-CF@rGO, rGO nanosheets (400 mg) were dispersed in 30 mL of DMF solvent followed by the gradual addition of metal precursors such as $Cu(acac)_2$ (40 mg), $Fe(acac)_3$ (240 mg), and $Au(acac)_3$ (40 mg) into the above mixture and stir to attain a homogeneous solution. The obtained paste was then kept in the oven at 130 °C until dried solid samples formed before their careful collection and grinding for 30 min to obtain a homogenous powder mixture. Lastly, the ground material was sintered under N_2 atm at 350 °C for 2 h to produce the final Au-CF@rGO. Similar procedures were followed to obtain CF@rGO and Au@rGO with their corresponding precursors. The detailed synthetic procedure of the development of Au-CF@rGO was represented in Scheme 1.

2.3. Fabrication of the modified electrodes

Initially, the active surface of GCE electrode was well polished with 0.05 µM alumina slurry several times and further cleaned with DI water and ethanol by ultrasonication. Then the cleaned GCE electrode was kept in a hot air oven to maintain dryness. 8 µL of the Au-CF@rGO nanomaterial slurry was drop-casted over the polished GCE surface and dried under a N_2 atm. CF@rGO/GCE and Au@ rGO/GCE modified electrodes were fabricated using the same procedures.

2.4. Material characterization

The as-synthesized Au@rGO, CF@rGO, and Au-CF@rGO samples were characterized by X-ray diffractometry (XRD, RigakuUltima), Raman spectroscopy (LabRam ARAMIS IR2), X-ray photoelectron spectroscopy (XPS, ULVAC-PHI), field emission scanning electron microscopy (FE-SEM, Quanta 25 FEG; FEI), high resolution-transmission electron microscopy (HR-TEM, JEM-2010; JEOL), atomic force microscopy (AFM, XE-100), and N_2 adsorption and desorption isotherms (Micromeritics, ASAP 2020).

2.5. Electrochemical measurements

The electrochemical characterization of the prepared Au-CF@rGO/GCE electrode was interrogated using a Biologic electrochemical workstation (VSP-300). The fabricated modified electrode is used as the working electrode, Pt rod as a counter electrode, and a Ag|AgCl as the reference electrode.

3. Results and discussion

3.1. Elemental characterization

The XRD and Raman spectroscopy results of the obtained rGO, CF@rGO, Au@rGO, and Au-CF@rGO are revealed in Fig. 1(a, b),

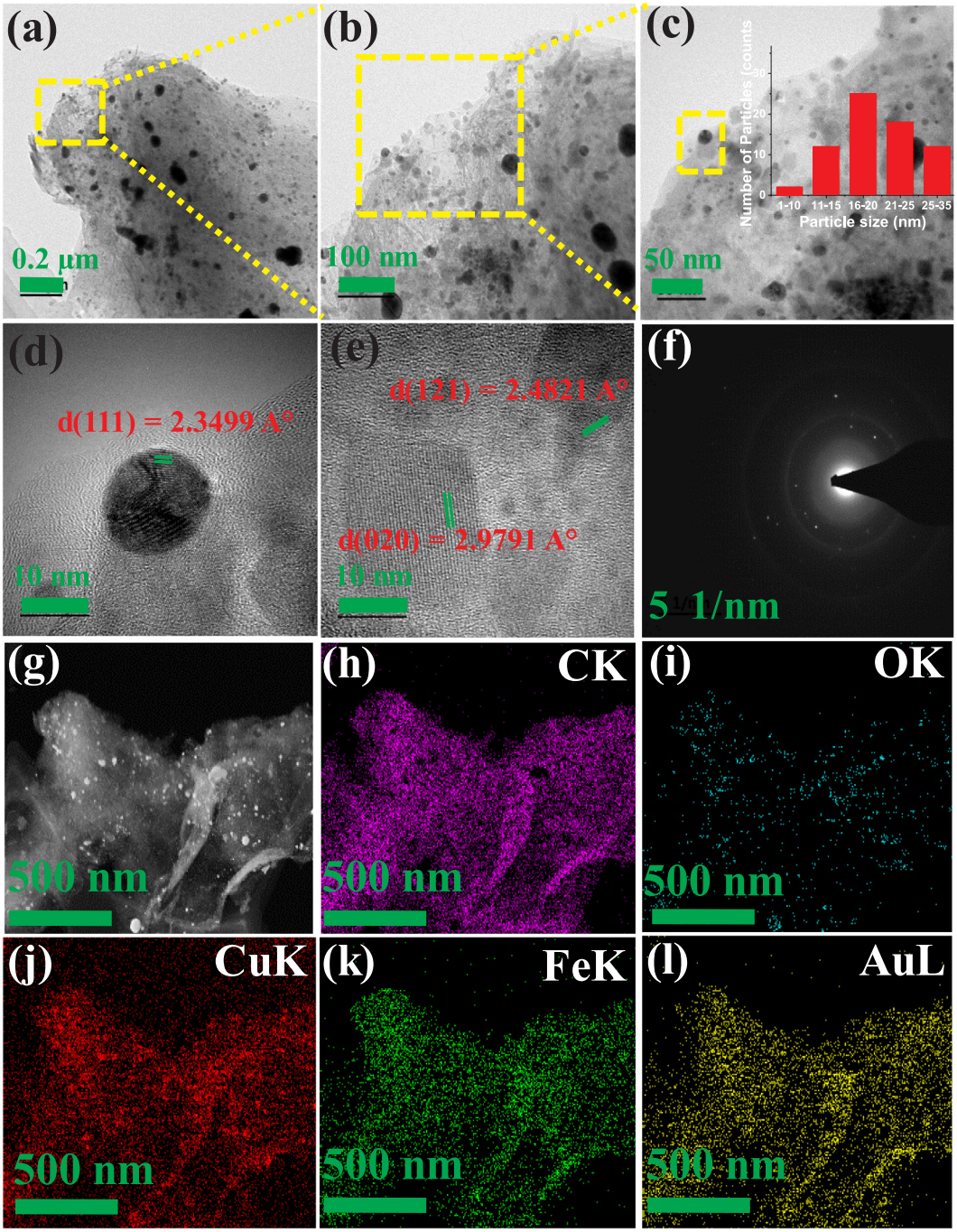

Fig. 4. (a–e) TEM images at low and high magnification of the prepared Au-CF@rGO. (f) Its corresponding SAED pattern, and (g–l) EDX elemental mapping of Au-CF@rGO, displaying the uniform distribution of C, O, Cu, Fe, and Au.

respectively. The main peak at around 2θ = ~23.5° agrees to the (002) plane of the rGO (Fig. 1a). During the US–DS, metallic gold nanoparticles are strongly anchored onto the rGO nanostructures and can be observed noticeably in the XRD patterns. The face-centered cubic (fcc) structure of the gold is evident from the peaks around 38°, 44°, 64°, and 77°, which agree to the (111), (200), (220), and (311) planes respectively (ICSD:53763). These results demonstrated the formation of Au@rGO by the US–DS from $Au(acac)_3$ and rGO. The procedure for forming $CuFe_2O_4$ using $Cu(acac)_2$, $Fe(acac)_3$, and rGO is given in detail in the experimental section. The diffraction peaks were well indexed and in accordance with the ICSD:16666 data for the tetragonal phase of $CuFe_2O_4$ [50]. Furthermore, the formation of the trimetallic carbon nanostructures shows major diffraction peaks of both metallic Au and CF (Fig. 1 (a)). The XRD analysis confirms that Au@rGO, CF@rGO, and Au-CF@rGO nanostructured materials prepared by the US–DS demonstrate high crystallinity and excellent phase purity.

Raman spectra were used to evaluate the defects present in the rGO, CF@rGO, Au@rGO, and Au-CF@rGO samples as shown in Fig. 1(b). Two main Raman peaks agreeing to the D and G bands of rGO were observed at 1365 and 1580 cm^{-1} respectively. I_D/I_G ratios were calculated for the rGO (0.397), Au@rGO (0.532), CF@rGO (1.12), and Au-CF@rGO (1.267). The defects observed in each sample can be attributed to the presence of single, bimetallic, and trimetallic particles that strongly interact with the rGO nanostructures. The presence of higher defects generates more active sites on rGO nanosheets that afford numerous active sensing sites for sensing during the electrochemical

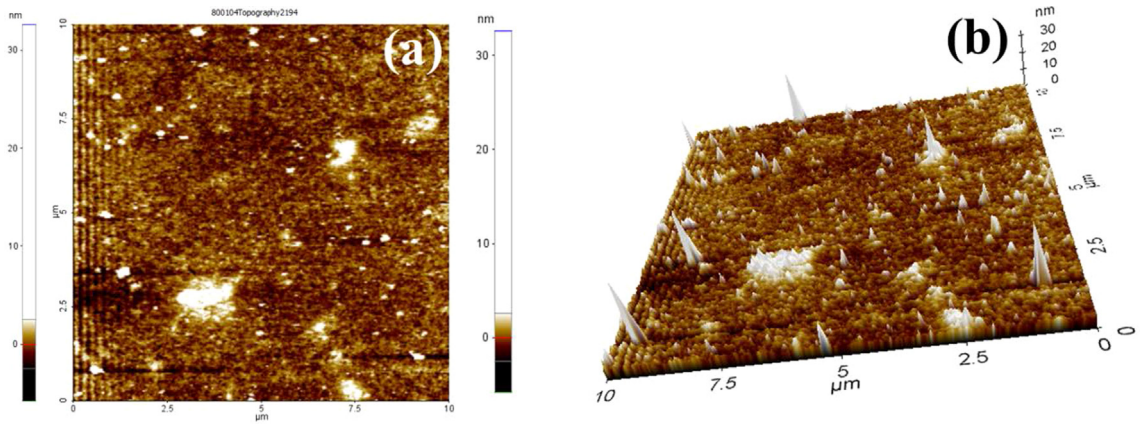

Fig. 5. (a) 2-D and (b) 3-D AFM images of A-CF@rGO.

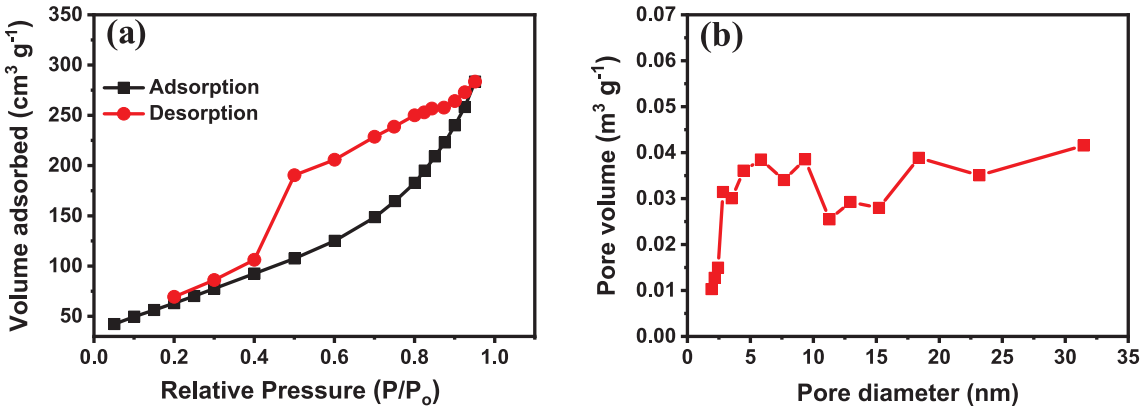

Fig. 6. (a) Nitrogen adsorption/desorption isotherm and (b) Pore. size distribution of Au-CF@rGO.

reactions. Furthermore, the mono-, bi-, and tri-metallic nanomaterials present in the nanostructure matrix may enhance the electrocatalytic activity[47,48].

Furthermore, to verify the elemental composition and oxidation states of the US–DS synthesized Au-CF@rGO material by XPS analysis and depicted in Fig. 2 (a–f). In the survey spectrum, the presence of C1s, O1s, Cu 2p, Fe 2p, and Au 4f peaks confirm the formation of Au-CF@rGO (Fig. 2(a)). The four deconvoluted peaks of the C 1 s belong to C = C, C-C, C-O, and O-C-O at 284.2, 284.8, 285.4, and 288.7 eV, respectively (Fig. 2(b)). The O1s spectrum has two deconvoluted peaks at around 529.4 and 531.4 eV well agreement with O^{2-} and OH^{-}, respectively (Fig. 2(c)). The high-resolution Cu 2p can be deconvoluted into two peaks at 933.5 eV and 954.2 eV respectively, associated with Cu^{2+} satellite peak around 943.3 eV (Fig. 2(d). The Fe 1 s spectrum shows a peak at 710.9 eV and 724.6 eV that can be correspond to the Fe^{3+} of the Fe $2p_{3/2}$ and Fe $2p_{1/2}$, respectively (Fig. 2(e) [51,52]. The obtained XPS results confirm the formation of $CuFe_2O_4$ in the rGO matrix. Moreover, the deconvolution of Au 4f into two symmetrical peaks at 84.0 eV ($4f_{7/2}$) and 87.7 eV ($4f_{5/2}$) corresponds to Au^0 (Fig. 2(f)). The peak position and symmetry of these peaks are in good agreement with metallic gold strongly attached to the surface of rGO, which agrees with the XRD data.

3.2. Morphological studies

FE-SEM image of the US-DS Au-CF@rGO, CF@rGO, and Au@rGO samples are revealed in Fig. 3 (a-c). The FE-SEM images of the prepared samples indicate a randomly aggregated, disordered structure of mono-, bi-, and tri-metallic nanoparticles anchored on GO sheets in a wrinkled and folded manner. This wrinkled structure could be due to oxidation of the carboxyl and hydroxyl groups present on the GO nanosheets. This morphological study shows that the mono-, bi-, and tri-metallic nanoparticles were successfully fixed on wrinkled and folded GO nanosheets.

Further, the US–DS prepared Au-CF@rGO nanostructure was examined by high magnification HR-TEM analysis, SAED, and EDX elemental mapping, and their images are shown in Fig. 4(a–l). In the high-resolution images (Fig. 4(a–e)), it can be observed that Au-CF nanoparticles (size ~ 15 nm) are strongly attached to the rGO nanosheets. The d (1 1 1) = 2.3499 Å represents the Au and d (0 2 0) = 2.9791 Å, d (1 2 1) = 2.4821 Å represents the CF in the prepared Au-CF@rGO samples. Both Au and CF are homogeneously well mixed and strongly connected to the carbon nanostructures. The strong attachment of the nanomaterials to the rGO matrix is due to the high-speed shock waves produced during the ultrasonication process. Moreover, the several concentric rings with many intense spots that are present in the SAED pattern clearly show that the anchored material has a polycrystalline nature Fig. 4(f). These results are in accordance with the XRD spectral data shown in Fig. 1. In addition, EDS mapping analysis data indicate that Au, Cu, Fe, O, and C are distributed homogenously throughout the matrix material Fig. 4(g–l).

Two-dimensional (2-D) and three-dimensional (3-D) surface topography was captured for the Au-CF@rGO sample and the topographs are shown in Fig. 5(a,b). From the 2-D and 3-D images, it can be observed that the prepared sample has a good surface roughness of the GO sheets, as well as the even loading of the sub-nanometer Au-CF nanoparticles on the rGO sheets. From the 3D AFM profile, the surface roughness value (Rf) of Au-CF@rGO was found to be 38.43 nm.

The specific surface area and pore size distribution of the prepared Au-CF@rGO sample was analyzed by Brunauer–Emmett–Teller (BET) and depicted in Fig. 6 (a&b). Fig. 6(a) shows the nitrogen adsorption and desorption isotherms indicating type-IV trait with obvious hysteresis loops, showing the presence of mesopores in Au-CF@rGO sample.

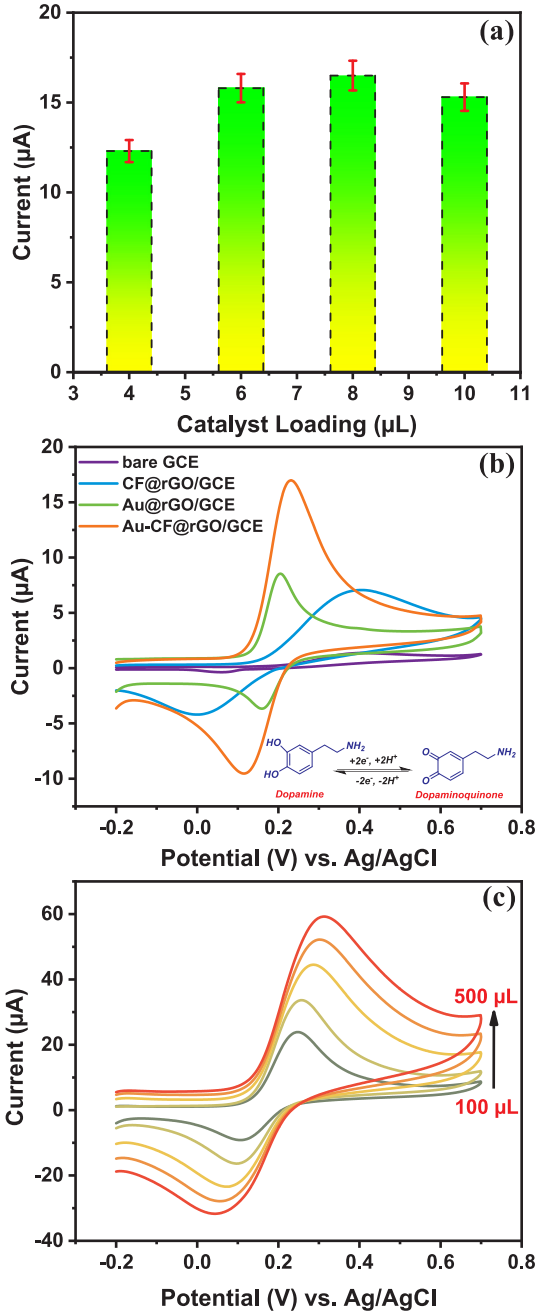

Fig. 7. (a) Effect of various (4, 6, 8, and 10 μL) Au-CF@rGO catalyst loadings (μg/μL) on the GCE electrode. (b) CV studies of the different catalytic electrodes of bare/GCE, CF@rGO/GCE, Au@rGO, and Au-CF@rGO/GCE in a PBS (pH 7) electrolyte solution with 100 μL DA at a scan rate of 50 mV/s (inset shows a possible reaction mechanism of DA oxidation). (c) CV obtained for the Au-CF@rGO/GCE electrode for various amounts of DA (100–500 μL) added in the nitrogen-saturated PBS electrolyte.

The specific surface area of the prepared Au-CF@rGO sample was found to be 288 m^2g^{-1}. The average pore size of the prepared Au-CF@rGO sample was determined to be 4.3 nm (Fig. 6(b)), indicating the presence of mesopores in the prepared sample. The presence of high surface area obviously corresponds to more active sites, directly supporting the high sensitivity of the sample.

3.3. Electrocatalytic activity of Au-CF@rGO-GCE toward DA detection

The as-prepared bare CGE, Au@rGO/GCE, CF@rGO/GCE, and Au-CF@rGO/GCE electrodes were evaluated by cyclic voltammetry (CV) toward DA detection using a three-electrode system with the aid of a PBS electrolyte. Prior to the electrochemical analysis, optimization studies for catalyst loading were performed to detect the accurate amount of DA, as the quantity of material on the GCE can affect the anodic/cathodic peak current and peak potential. Therefore, loading of the Au-CF@rGO suspension was optimized first by CV using Au-CF@rGO/GCE in the presence of PBS which contains 100 μL DA at a sweep rate of 50 mV/s. The obtained anodic peak current response (bar graph) is displayed in Fig. 7(a). The highest oxidation peak was observed with 8 μL of catalyst. There is an incremental in anodic peak current from 4 to 8 μL catalyst loading, indicating the active involvement of the Au-CF@rGO modifier in the electrochemical oxidation of DA. Increasing the loading amount beyond 8 μL slightly decreases the current response due to the agglomeration of the particles on the GCE surface. This agglomeration impedes electron movement, resulting in the anodic peak current decrease. Therefore, an 8 μL suspension of the Au-CF@rGO modifier was used as the optimized loading concentration for detecting the electrochemical properties of DA for further studies.

The electrochemical properties of Au-CF@rGO/GCE were studied under the optimized conditions using CV analysis of DA and comparisons with the other electrodes (bare GCE, Au@rGO/GCE, and CF@rGO/GCE) were performed in same experimental procedures. The CV response of the bare GCE, Au@rGO/GCE, CF@rGO/GCE, and Au-CF@rGO/GCE in a PBS solution containing 100 μL DA (pH 7) at a scan rate of 50 mV/s are depicted in Fig. 7(b). Due to poor interaction with electroactive species on the bare GCE, no redox peaks were observed with that system. In addition, the GCE modified with CF@rGE showed a small redox response along with an observed negative shift for the oxidation of DA due to the poor electron transfer behavior of CF@rGO. The Au@rGO/GCE modified electrode exhibited well-defined redox peaks, indicative of the excellent electron transfer behavior of the Au NPs on the rGO surface producing the lowest oxidation/reduction peak currents.

Among all electrodes, the Au-CF@rGO/GCE modified electrode exhibited robust and well-defined redox peaks at 0.228 V (E_{pa}, oxidation of DA to dopamine quinone (DAQ)) and 0.118 V (E_{pc}, reduction of DAQ to DA). The corresponding oxidation and reduction reaction pathways of DA during these electrochemical reactions are depicted in the inset of Fig. 7(b). Compared with other modified electrodes in this present study, the Au-CF@rGO/GCE electrode exhibit superior electrochemical performance toward DA redox behavior. Thus, the increased current response of DA on Au-CF@rGO/GCE can be ascribed to better conductivity, high specific area, and quick response of the Au nanoparticles.

To further verify the higher electrocatalytic activity of Au-CF@rGO/GCE, CV was performed with PBS containing different concentrations of DA (100–500 μL) in a fixed scan rate (50 mV/s) and the obtained results were depicted in Fig. 7(c). The obtained results are clearly indicating that a higher concentration of DA produces a steady-state redox peak current with a trivial discrepancy in the peak potentials. This demonstrates the higher electrocatalytic activity of Au-CF@rGO/GCE toward the electrochemical detection of DA.The electrochemical performance and elect catalyst activity of DA over Au-CF@rGO/GCE varied depending on the applied sweep rate and electrolyte solution pH. Therefore, CV was performed using Au-CF@rGO/GCE while varying the scan rate form 10–200 mV/s with PBS containing 100 μM of DA (pH 7). The obtained results are depicted in Fig. 8(a). From these results the scan rate increased from 10 to 200 mV/s, the resultant anodic peak uniformly increased with a trivial shift in the potential. The redox behavior and the corresponding peak potential change prove that the electrochemical oxidation process of DA is strongly consistent with the scan rate.

Furthermore, linear relationships between the (scan rate)$^{1/2}$ vs anodic (I_{pa}) and cathodic (I_{pc}) peak currents were noted, with correlation coefficients (R^2) of 0.9993 and 0.9796, respectively and exhibited

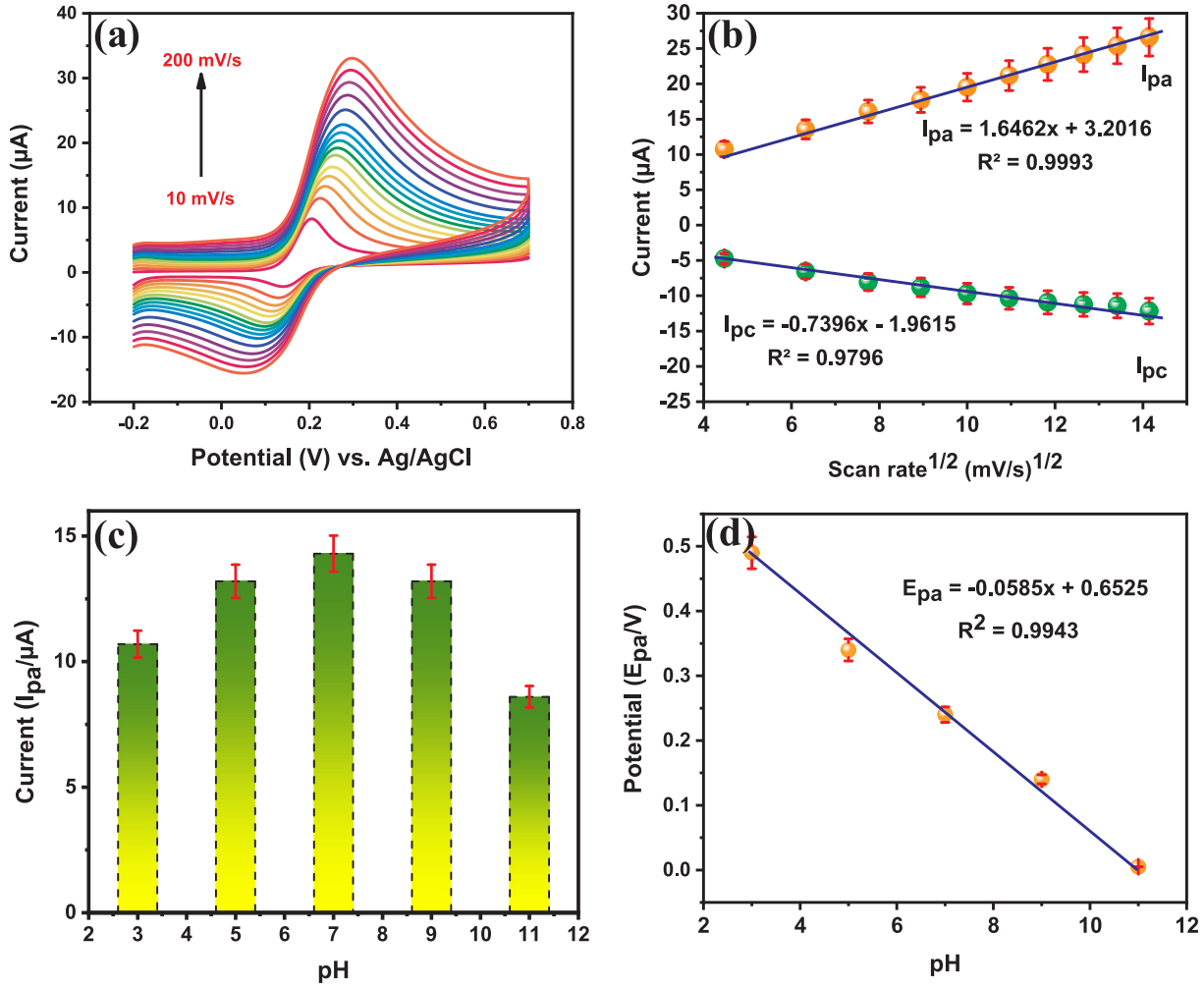

Fig. 8. (a) CV response of the Au-CF@rGO/GCE electrode with various scan rates from 10 to 200 mV/s in PBS electrolyte containing 100 μM DA. (b) Corresponding calibration plots (c) Bar graph of the CV response of the Au-CF@rGO/GCE electrode at various pH ranging from 3 to 11, and (d) corresponding calibration plot for pH vs. E_{pa}.

in Fig. 8(b). The correlation coefficients for the I_{pa} and I_{pc} peak currents are nearly equal to 1, indicating that the electrochemical behavior of DA is a diffusion-controlled process over the Au-CF@rGO/GCE [46,53]. Furthermore, analysis of the electrochemical properties of DA (100 μL) at various pH, ranging from 3 to 11, was carried out by CV analysis at a constant scan rate (50 mV/s) and represented in Fig. 8(c). Among the various pH, the highest oxidation peak was perceived in pH 7 indicating the electroactive species are most active in neutral pH medium (around 7). Lower anodic peak currents were observed above and below pH 7, indicating the instability of DA in both acidic and basic media. The formal potential (E^0) has a linear relationship toward DA over the pH range from 3 to 11 and 58.5 mV/pH fitting value was attained, which was closely correlated to the Nernst theoretical value of 59 mV/pH (Fig. 8(d)) [54,55]. The results are in accordance with the theoretical value and indicate an equivalent quantity of electrons and protons transferred during the electrochemical reactions. From this study implies that the prepared Au-CF@rGO modified electrode is two electrons and two protons transfer process during the electrochemical process of DA oxidation. Differential pulse voltammetry (DPV) is a more sensitive technique to accurately determine electrochemical responses at low concentration levels of small molecules. Therefore, low-level concentrations of DA were further assessed using DPV with the synthesized Au-CF@rGO/GCE. Fig. 9(a) describes the DVP response of DA using concentrations of 0.001–119.6 μM DA in a nitrogen saturated PBS solution (pH 7) using the Au-CF@rGO/GCE electrode. The lower limit of 0.001 μM DA displayed an oxidation peak that linearly increased upon DA addition to 119.2 μM due to the higher electrocatalytic activity of DA with Au-CF@rGO/GCE.

Furthermore, the corresponding calibration plot of the I_{pa} vs DA concentrations (μM) was fit and is depicted in Fig. 9(b). The linear relationship was noted with the linear regression equation $I_{pa} = 0.0129x + 0.4382$, $R^2 = 0.9938$. The linear response range was determined to be 0.001–107.1 μM. The LOD was calibrated to be 0.34 nM using the standard equation of 3σ/S [56–58]. The calculated sensitivity is 8.743 $\mu A \mu M^{-1} cm^{-2}$. The calculated analytical parameters are compared to the previously reported DA sensor parameters and are summarized in Table 1. From these overall results, the US–DS route of preparing Au-CF@rGO was found to produce better results and higher electrocatalytic response for the detection of DA. The superior electrochemical performances of the Au-CF@rGO material is mainly because of the presence of active defect sites, the nano sized catalytic particles, the larger surface area, and the good metal-support interactions. In addition, the US–DS method assisted the homogenous dispersion of catalytic nanoparticles anchored on the active defect cites of the rGO surface.

To evaluate the practical feasibility, selectivity, stability, repeatability, and reproducibility of Au-CF@rGO/GCE, it was further assessed by DPV in the same conditions. The selectivity of the electrochemical sensor was evaluated by DPV in various small biological molecules such as ascorbic acid (AA), glucose (Glu), hydrogen peroxide (H_2O_2), folic

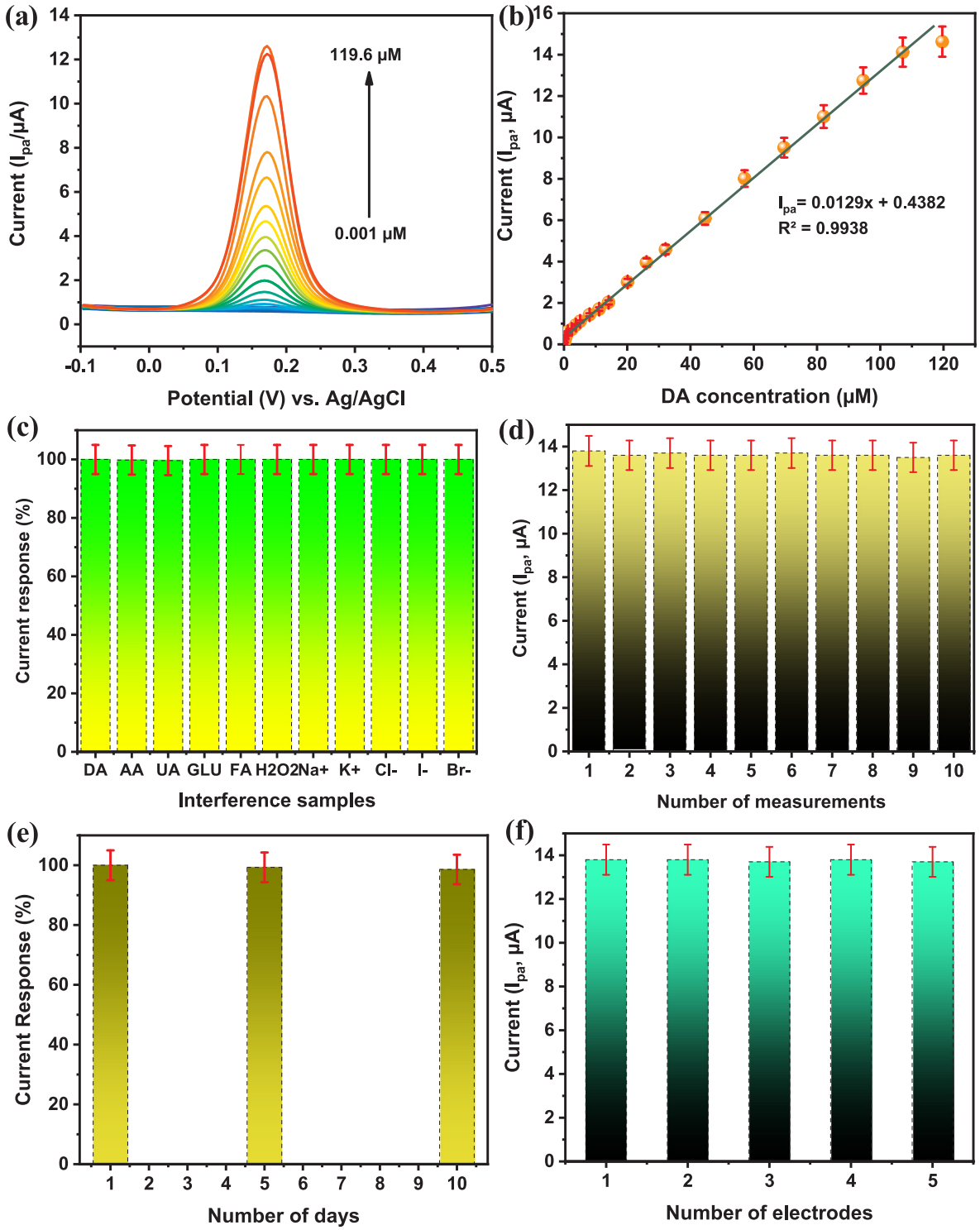

Fig. 9. (a) DPV current response for different concentrations from 0.001 to 119.6 μM in nitrogen saturated PBS solution; (b) Corresponding calibration plot for various DA concentrations vs I_{pa} (μA); (c) DPV analysis of the fabricated Au-CF@rGO/GCE sensor with different interfering species, (d) repeatability, (e) storage stability, and (f) fabrication stability of the Au-CF@rGO/GCE sensor for DA detection.

acid (FA), uric acid (UA), and metal ions, including Na^+, K^+, Cl^-, I^-, and Br^-. Fig. 9(c) shows the DPV's current response of DA, 20-fold higher concentrations of small molecules, and 50-fold higher concentrations of metal ions. Noted that, there is no significant change (< 1%) in the oxidation peak current, indicating the excellent utility of the DA sensor using Au-CF@rGO/GCE. Further, the repeatability of Au-CF@rGO/GCE was examined by DPV measurements in 10 different electrolyte systems (PBS, pH 7), and the obtained current responses are presented in Fig. 9(d). The relative standard deviation (RSD) value was found to be 4.1% (n = 3). In addition, Au-CF@rGO/GCE was used for DPV after a time interval of five days is depicted in Fig. 9(e). There was no significant change in the current response (< 5%) detected until an interval of 10 days, demonstrating the excellent storage stability for the modified electrochemical sensor. In addition, five different electrodes were evaluated in a PBS electrolyte (pH 7), and the results are revealed in Fig. 9(f). An RSD of 4.6% was obtained. It can thus be concluded that

Table 1
Comparison of DA detection by the DPV method for Au-CF@rGO nanomaterial prepared by US-DS compared with various sensor materials developed via different synthetic routes.

Electrode Material	Synthesis Route	Range (μM)	LOD (nm)	Reference
NiO–CuO/GR/GCE	Electrodeposition	0.3–40	100	[59]
Mesoporous $ZnFe_2O_4$	Facial nanocasting	0.002–0.6	0.4	[9]
TiC/CNFs	Electrospinning	0.05–45	20	[60]
AuNPs@MoS_2-NSs	Reduction process	5.0–200	1000	[34]
Flower shaped ZnO	Aqueous solution	0.1—16	40	[61]
Al polished GCE	Alumina Polishing	0.15–25.25	46	[55]
Graphite/Gelatin	Sonochemical	0.05–79.5	4.5	[53]
Fullerene/PdNPs	Screen Printing	0.35–150.55	56	[62]
Au-Cu_2O/rGO	Wet chemical	10–90	3900	[33]
Pt–Ag/Gr	Chemical method	0.1–60	12	[10]
polyaniline/rGO	Hydrothermal	0.05–10	24	[63]
PdAu/rGO	Facile method	1.25–73.75	750	[64]
Au-CF@rGO	US–DS	0.001–119.9	0.34	This work

Table 2
Real sample analysis.

Real sample	Added (μM)	Found (μM)	Recovery (%)	*RSD (%)
Banana milk 1	10	9.9	99	3.02
	20	19.7	98.5	3.14
Banana milk 2	10	9.7	97	2.98
	20	19.8	99	3.16

* RSD = number of measurement (n = 3).

the Au-CF@rGO/GCE system possesses good stability, excellent reproducibility, and acceptable repeatability for use as a DA sensor. To evaluate possible practical applications, a real sample analysis of DA was conducted using Au-CF@rGO/GCE as an electrode with banana milk (available commercially), purchased from a local convenience store in the Republic of Korea. DPV was used for analyzing these real samples via a standard addition method. The recovery values obtained are listed in Table 2. An appreciable recovery ranging from 97 to 99% was achieved, suggesting that Au-CF@rGO/GCE is a promising material for the analysis of real samples.

4. Conclusion

In summary, we successfully synthesized Au-CF@rGO by the US followed by DS. The successful formation of the Au-CF nanoparticles and their composition, crystallinity, and uniform distribution over the rGO sheet was observed by XRD, XPS, Raman, FE-SEM, HR-TEM, and EDS analyses. Further, the modified Au-CF@rGO/GCE electrode was examined by various electrochemical analyses, and the Au-CF@rGO/GCE modified electrode showed excellent activity toward DA detection. Interestingly, higher peak currents with lower anodic potentials were revealed by the fabricated Au-CF@rGO/GCE modified electrode with a broader linear range of 0.001–119.6 μM, a lower detection limit of 0.001 μM, a LOD of 0.34 nM, and greater sensitivity of 8.743 $\mu A \mu M^{-1} cm^{-2}$. Moreover, the prepared sensor exhibited excellent reproducibility and selectivity toward biological molecules and is thus a possible alternative for a dopamine-detecting electrochemical sensor.

CRediT authorship contribution statement

Vijayakumar Elayappan: Writing - original draft, Writing - review & editing, Data curation. **Selvaganapathy Muthusamy:** Data curation. **Gopiraman Mayakrishnan:** Data curation. **Ramkumar Balasubramaniam:** Resources. **Yun-Sung Lee:** Resources. **Hyun Sung Noh:** Resources. **Dawool Kwon:** Resources. **Mtangi Mohamed Mussa:** Resources. **Haigun Lee:** Writing - review & editing.

Declaration of Competing Interest

The authors declare that they have no known competing financial interests or personal relationships that could have appeared to influence the work reported in this paper.

Acknowledgments

This work is supported by the Korea Basic Science Institute (KBSI) Grant No. D010200 and in part by the Brain Korea 21 Plus Project in 2020.

References

[1] R. Ramachandran, T.-W. Chen, S.-M. Chen, T. Baskar, R. Kannan, P. Elumalai, P. Raja, T. Jeyapragasam, K. Dinakaran, G. Peter Gnana Kumar, A review of the advanced developments of electrochemical sensors for the detection of toxic and bioactive molecules, Inorg. Chem.Front 6 (2019) 3418–3439, https://doi.org/10.1039/c9qi00602h.
[2] F.B. Kamal Eddin, Y. Wing Fen, Recent advances in electrochemical and optical sensing of dopamine, Sensors (Basel) 20 (2020) 1–47, https://doi.org/10.3390/s20041039.
[3] M.M. Rahman, J.J. Lee, Electrochemical dopamine sensors based on graphene, J. Electrochem. Sci. Technol. 10 (2019) 185–195, https://doi.org/10.5229/JECST.2019.10.2.185.
[4] X. Liu, Y. Fu, Q. Sheng, J. Zheng, Au nanoparticles attached Ag@C core-shell nanocomposites for highly selective electrochemical detection of dopamine, Microchem. J. 146 (2019) 509–516, https://doi.org/10.1016/j.microc.2019.01.023.
[5] X. Sun, L. Zhang, X. Zhang, X. Liu, J. Jian, D. Kong, D. Zeng, H. Yuan, S. Feng, Electrochemical dopamine sensor based on superionic conducting potassium ferrite, Biosens. Bioelectron. 153 (2020) 112045, , https://doi.org/10.1016/j.bios.2020.112045.
[6] M. Zhao, Z. Li, X. Zhang, J. Yu, Y. Ding, H. Li, Y. Ma, Employing the interfacial barrier of P-rGO/ZnO microspheres for improving the electrochemical sensing performance to dopamine, Sens. Actuat., B Chem. 309 (2020) 1277572, https://doi.org/10.1016/j.snb.2020.127757.
[7] C. Ben Ali Hassine, H. Kahri, H. Barhoumi, Enhancing dopamine detection using glassy carbon electrode modified with graphene oxide, nickel and gold nanoparticles, J. Electrochem. Soc. 167 (2020), https://doi.org/10.1149/1945-7111/ab6971 027516.
[8] Z. Lu, Y. Li, T. Liu, G. Wang, M. Sun, Y. Jiang, H. He, Y. Wang, P. Zou, X. Wang, Q. Zhao, H. Rao, A dual-template imprinted polymer electrochemical sensor based on AuNPs and nitrogen-doped graphene oxide quantum dots coated on NiS_2/biomass carbon for simultaneous determination of dopamine and chlorpromazine, Chem. Eng. J. 389 (2020), https://doi.org/10.1016/j.cej.2020.124417 124417.
[9] Y. Huang, Y. Tang, S. Xu, M. Feng, Y. Yu, W. Yang, H. Li, A highly sensitive sensor based on ordered mesoporous $ZnFe_2O_4$ for electrochemical detection of dopamine, Anal. Chim. Acta 1096 (2020) 26–33, https://doi.org/10.1016/j.aca.2019.10.048.
[10] N.S. Anuar, W.J. Basirun, M. Shalauddin, S. Akhter, A dopamine electrochemical sensor based on a platinum-silver graphene nanocomposite modified electrode, RSC Adv. 10 (2020) 17336–17344, https://doi.org/10.1039/c9ra11056a.
[11] J.M. Liu, X.X. Wang, M.L. Cui, L.P. Lin, S.L. Jiang, L. Jiao, L.H. Zhang, A promising non-aggregation colorimetric sensor of AuNRs-Ag+ for determination of dopamine, Sens. Actuat., B Chem 176 (2013) 97–102, https://doi.org/10.1016/j.snb.2012.08.083.
[12] Y. Leng, K. Xie, L. Ye, G. Li, Z. Lu, J. He, Gold-nanoparticle-based colorimetric array for detection of dopamine in urine and serum, Talanta 139 (2015) 89–95, https://doi.org/10.1016/j.talanta.2015.02.038.
[13] L. Guo, Y. Zhang, Q. Li, Spectrophotometric determination of dopamine hydrochloride in pharmaceutical, banana, urine and serum samples by potassium ferricyanide-Fe(III), Anal. Sci. 25 (2009) 1451–1455, https://doi.org/10.2116/analsci.25.1451.
[14] N. Rami Reddy, G. Sreedevi, K. Prabhavathi, I.E. Chakravarthy, Spectrophotometric determination of dopamine in pharmaceutical formulations, J. Anal. Chem. 60 (2005) 252–253, https://doi.org/10.1007/s10809-005-0080-3.
[15] A. Yildirim, M. Bayindir, Turn-on fluorescent dopamine sensing based on in situ formation of visible light emitting polydopamine nanoparticles, Anal. Chem. 86 (2014) 5508–5512, https://doi.org/10.1021/ac500771q.
[16] X. Chen, N. Zheng, S. Chen, Q. Ma, Fluorescence detection of dopamine based on nitrogen-doped graphene quantum dots and visible paper-based test strips, Anal. Methods 9 (2017) 2246–2251, https://doi.org/10.1039/c7ay00028f.
[17] L. Li, H. Liu, Y. Shen, J. Zhang, J.J. Zhu, Electrogenerated chemiluminescence of Au nanoclusters for the detection of dopamine, Anal. Chem. 83 (2011) 661–665, https://doi.org/10.1021/ac102623r.
[18] X. Wang, Y. Ma, X. Yao, J. Wang, M. Yin, Determination of dopamine in rat less differentiated pheochromocytoma cells by capillary electrophoresis with a palladium nanoparticles microdisk electrode, RSC Adv. 3 (2013) 24605–24611, https://

doi.org/10.1039/c3ra44481c.
[19] H. Gu, E.L. Varner, S.R. Groskreutz, A.C. Michael, S.G. Weber, In vivo monitoring of dopamine by microdialysis with 1 min temporal resolution using online capillary liquid chromatography with electrochemical detection, Anal. Chem. 87 (2015) 6088–6094, https://doi.org/10.1021/acs.analchem.5b00633.
[20] Y. Lu, J.L. Peters, A.C. Michael, Direct comparison of the response of voltammetry and microdialysis to electrically evoked release of striatal dopamine, J. Neurochem. 70 (2002) 584–593, https://doi.org/10.1046/j.1471-4159.1998.70020584.x.
[21] M. Jalali, E. Filine, S. Dalfen, S. Mahshid, Microscale reactor embedded with Graphene/hierarchical gold nanostructures for electrochemical sensing: application to the determination of dopamine, Microchim. Acta 187 (2020), https://doi.org/10.1007/s00604-019-4059-4.
[22] V. Elayappan, R. Shanmugam, S. Chinnusamy, D.J. Yoo, G. Mayakrishnan, K. Kim, H.S. Noh, M.K. Kim, H. Lee, Three-dimensional bimetal TMO supported carbon based electrocatalyst developed via dry synthesis for hydrogen and oxygen evolution, Appl. Surf. Sci. 505 (2020) 144642, , https://doi.org/10.1016/j.apsusc.2019.144642.
[23] S. Ambika, S. Gopinath, K. Saravanan, K. Sivakumar, C. Ragupathi, T.A. Sukantha, Structural, morphological and optical properties and solar cell applications of thioglycolic routed nano cobalt oxide material, Energy Rep. 5 (2019) 305–309, https://doi.org/10.1016/j.egyr.2019.02.005.
[24] M.A.A. Mohd Abdah, N.H.N. Azman, S. Kulandaivalu, Y. Sulaiman, Review of the use of transition-metal-oxide and conducting polymer-based fibres for high-performance supercapacitors, Mater. Des. 186 (2020) 108199, , https://doi.org/10.1016/j.matdes.2019.108199.
[25] C. An, Y. Zhang, H. Guo, Y. Wang, Metal oxide-based supercapacitors: progress and prospectives, Nanoscale Adv. 1 (2019) 4644–4658, https://doi.org/10.1039/c9na00543a.
[26] Q. Liu, Z. Hu, M. Chen, C. Zou, H. Jin, S. Wang, S.L. Chou, S.X. Dou, Recent progress of layered transition metal oxide cathodes for sodium-ion batteries, Small 15 (2019) 1–24, https://doi.org/10.1002/smll.201805381.
[27] L.S.K. Achary, A. Kumar, B. Barik, P.S. Nayak, N. Tripathy, J.P. Kar, P. Dash, Reduced graphene oxide-$CuFe_2O_4$ nanocomposite: A highly sensitive room temperature NH_3 gas sensor, Sens. Actuat., B Chem. 272 (2018) 100–109, https://doi.org/10.1016/j.snb.2018.05.093.
[28] J. Wu, Z. Li, X. Xie, K. Tao, C. Liu, K.A. Khor, J. Miao, L.K. Norford, 3D superhydrophobic reduced graphene oxide for activated NO_2 sensing with enhanced immunity to humidity, J. Mater. Chem. A 6 (2018) 478–488, https://doi.org/10.1039/c7ta08775f.
[29] A. Lipatov, A. Varezhnikov, P. Wilson, V. Sysoev, A. Kolmakov, A. Sinitskii, Highly selective gas sensor arrays based on thermally reduced graphene oxide, Nanoscale 5 (2013) 5426–5434, https://doi.org/10.1039/c3nr00747b.
[30] K. Dhara, T. Ramachandran, B.G. Nair, T.G. Satheesh Babu, Au nanoparticles decorated reduced graphene oxide for the fabrication of disposable nonenzymatic hydrogen peroxide sensor, J. Electroanal. Chem. 764 (2016) 64–70, https://doi.org/10.1016/j.jelechem.2016.01.011.
[31] W. Wang, D. Zhang, Facile preparation of rGO/MFe2O4 (M = Cu Co, Ni) nanohybrids and its catalytic performance during the thermal decomposition of ammonium perchlorate, RSC Adv. 8 (2018) 32221–32230, https://doi.org/10.1039/c8ra04412k.
[32] S. Ghosh, Y. Holade, H. Remita, K. Servat, P. Beaunier, A. Hagège, K.B. Kokoh, T.W. Napporn, One-pot synthesis of reduced graphene oxide supported gold-based nanomaterials as robust nanocatalysts for glucose electrooxidation, Electrochim. Acta 212 (2016) 864–875, https://doi.org/10.1016/j.electacta.2016.06.169.
[33] T.K. Aparna, R. Sivasubramanian, M.A. Dar, One-pot synthesis of Au-Cu_2O/rGO nanocomposite based electrochemical sensor for selective and simultaneous detection of dopamine and uric acid, J. Alloy. Compd. 741 (2018) 1130–1141, https://doi.org/10.1016/j.jallcom.2018.01.205.
[34] H.L. Zou, B.L. Li, H.Q. Luo, N.B. Li, 0D–2D heterostructures of Au nanoparticles and layered MoS_2 for simultaneous detections of dopamine, ascorbic acid, uric acid, and nitrite, Sens. Actuat., B Chem. 253 (2017) 352–360, https://doi.org/10.1016/j.snb.2017.06.158.
[35] S. Ida, P. Wilson, B. Neppolian, M. Sathish, A.R. Mahammed Shaheer, P. Ravi, Tuning the type of nitrogen on N-RGO supported on N-TiO_2 under ultrasonication/hydrothermal treatment for efficient hydrogen evolution – A mechanistic overview, Ultrason. Sonochem. 64 (2020) 104866, , https://doi.org/10.1016/j.ultsonch.2019.104866.
[36] S. Ida, P. Wilson, B. Neppolian, M. Sathish, P. Karthik, P. Ravi, Ultrasonically aided selective stabilization of pyrrolic type nitrogen by one pot nitrogen doped and hydrothermally reduced Graphene oxide/Titania nanocomposite (N-TiO_2/N-RGO) for H_2 production, Ultrason. Sonochem. 57 (2019) 62–72, https://doi.org/10.1016/j.ultsonch.2019.04.041.
[37] W. Zhang, Y. Yang, E. Ziemann, A. Be'Er, M.Y. Bashouti, M. Elimelech, R. Bernstein, One-step sonochemical synthesis of a reduced graphene oxide-ZnO nanocomposite with antibacterial and antibiofouling properties, Environ. Sci. Nano 6 (2019) 3080–3090, https://doi.org/10.1039/c9en00753a.
[38] A.M. Golsheikh, N.M. Huang, H.N. Lim, R. Zakaria, One-pot sonochemical synthesis of reduced graphene oxide uniformly decorated with ultrafine silver nanoparticles for non-enzymatic detection of H_2O_2 and optical detection of mercury ions, RSC Adv. 4 (2014) 36401–36411, https://doi.org/10.1039/c4ra05998k.
[39] J.H. Bang, K.S. Suslick, Applications of ultrasound to the synthesis of nanostructured materials, Adv. Mater. 22 (2010) 1039–1059, https://doi.org/10.1002/adma.200904093.
[40] S. Alizadeh, N. Fallah, M. Nikazar, An ultrasonic method for the synthesis, control and optimization of CdS/TiO_2 core-shell nanocomposites, RSC Adv. 9 (2019) 4314–4324, https://doi.org/10.1039/c8ra10155h.
[41] M. Joharian, A. Morsali, Ultrasound-assisted synthesis of two new fluorinated metal-organic frameworks (F-MOFs) with the high surface area to improve the catalytic activity, J. Solid State Chem. 270 (2019) 135–146, https://doi.org/10.1016/j.jssc.2018.10.046.
[42] M. Tanhaei, A.R. Mahjoub, V. Safarifard, Ultrasonic-assisted synthesis and characterization of nanocomposites from azine-decorated metal-organic framework and graphene oxide layers, Mater. Lett. 227 (2018) 318–321, https://doi.org/10.1016/j.matlet.2018.04.130.
[43] Y. Luo, S. Fan, N. Hao, S. Zhong, W. Liu, An ultrasound-assisted approach to synthesize Mn_3O_4/RGO hybrids with high capability for lithium ion batteries, Dalt Trans. 43 (2014) 15317–15320, https://doi.org/10.1039/c4dt01695e.
[44] P. Sundaresan, A. Yamuna, S.M. Chen, Sonochemical synthesis of samarium tungstate nanoparticles for the electrochemical detection of nilutamide, Ultrason. Sonochem. 67 (2020) 105146, , https://doi.org/10.1016/j.ultsonch.2020.105146.
[45] T.W. Chen, R. Arumugam, S.M. Chen, M. Altaf, S. Manohardas, M. Saeed Ali Abuhasil, M. Ajmal Ali, Ultrasonic preparation and nanosheets supported binary metal oxide nanocomposite for the effective application towards the electrochemical sensor, Ultrason. Sonochem. 64 (2020), https://doi.org/10.1016/j.ultsonch.2020.105007 105007.
[46] B. Arumugam, B. Muthukutty, S.M. Chen, S. Kannan Ramaraj, J. Vinoth Kumar, E.R. Nagarajan, Ultrasonication-aided synthesis of nanoplates-like iron molybdate: Fabricated over glassy carbon electrode as an modified electrode for the selective determination of first generation antihistamine drug promethazine hydrochloride, Ultrason. Sonochem. 66 (2020), https://doi.org/10.1016/j.ultsonch.2020.104977 104977.
[47] G. Mayakrishnan, S. Somasundaram, D. Dian, A. Ilangovan, I.S. Kim, I.M. Chung, Facile mechanochemical synthesis of nickel/graphene oxide nanocomposites with heterogeneous catalysis and supercapacitors, Catalysts 9 (2019) 486.
[48] M. Gopiraman, D. Deng, S.G. Babu, T. Hayashi, R. Karvembu, I.S. Kim, Sustainable and versatile CuO/GNS nanocatalyst for highly efficient base free coupling reactions, ACS Sustain. Chem. Eng. 3 (2015) 2478–2488, https://doi.org/10.1021/acssuschemeng.5b00542.
[49] Mayakrishnan Gopiraman, Sundaram Ganesh Babu, Zeeshan Khatri, Wei Kai, Yoong Ahm Kim, Morinobu Endo, Ramasamy Karvembu, Ick Soo Kim, Dry Synthesis of Easily Tunable Nano Ruthenium Supported on Graphene: Novel Nanocatalysts for Aerial Oxidation of Alcohols and Transfer Hydrogenation of Ketones, J. Phys. Chem. C 117 (45) (2013) 23582–23596, https://doi.org/10.1021/jp402978q.
[50] S.A. Soomro, I.H. Gul, H. Naseer, S. Marwat, M. Mujahid, Improved performance of cufe2o4/rgo nanohybrid as an anode material for lithium-ion batteries prepared via facile one-step method, Curr. Nanosci. 15 (2018) 420–429, https://doi.org/10.2174/1573413714666181115122016.
[51] M. Tang, F. Xia, C. Gao, H. Qiu, Preparation of magnetically recyclable $CuFe_2O_4$/RGO for catalytic hydrolysis of sodium borohydride, Int. J. Hydrogen Energy 41 (2016) 13058–13068, https://doi.org/10.1016/j.ijhydene.2016.05.034.
[52] C. Karthikeyan, K. Ramachandran, S. Sheet, D.J. Yoo, Y.S. Lee, Y. Satish Kumar, A.R. Kim, G. Gnana Kumar, Pigeon-excreta-mediated synthesis of reduced graphene oxide (rGO)/$CuFe_2O_4$ nanocomposite and its catalytic activity toward sensitive and selective hydrogen peroxide detection, ACS Sustain, Chem. Eng. 5 (2017) 4897–4905, https://doi.org/10.1021/acssuschemeng.7b00314.
[53] C. Rajkumar, B. Thirumalraj, S.M. Chen, H.A. Chen, A simple preparation of graphite/gelatin composite for electrochemical detection of dopamine, J. Colloid Interface Sci. 487 (2017) 149–155, https://doi.org/10.1016/j.jcis.2016.10.024.
[54] S.M. Chen, R. Umamaheswari, G. Mani, T.W. Chen, M.A. Ali, A.H. Fahad, M.S. Elshikh, M.A. Farah, Hierarchically structured $CuFe_2O_4$ND@RGO composite for the detection of oxidative stress biomarker in biological fluids, Inorg. Chem. Front. 5 (2018) 944–950, https://doi.org/10.1039/c7qi00799j.
[55] B. Thirumalraj, S. Palanisamy, S.M. Chen, R. Sayee Kannan, Alumina polished glassy carbon electrode as a simple electrode for lower potential electrochemical detection of dopamine in its sub-micromolar level, Electroanalysis 28 (2016) 425–430, https://doi.org/10.1002/elan.201500446.
[56] T.W. Chen, S. Chinnapaiyan, S.M. Chen, M. Ajmal Ali, M.S. Elshikh, A. Hossam Mahmoud, Facile synthesis of copper ferrite nanoparticles with chitosan composite for high-performance electrochemical sensor, Ultrason. Sonochem. 63 (2020) 104902, , https://doi.org/10.1016/j.ultsonch.2019.104902.
[57] B. Thirumalraj, C. Rajkumar, S.M. Chen, P. Barathi, Highly stable biomolecule supported by gold nanoparticles/graphene nanocomposite as a sensing platform for H_2O_2 biosensor application, J. Mater. Chem. B 4 (2016) 6335–6343, https://doi.org/10.1039/c6tb01576j.
[58] S. Kubendhiran, B. Thirumalraj, S.M. Chen, C. Karuppiah, Electrochemical co-preparation of cobalt sulfide/reduced graphene oxide composite for electrocatalytic activity and determination of H_2O_2 in biological samples, J. Colloid Interface Sci. 509 (2018) 153–162, https://doi.org/10.1016/j.jcis.2017.08.087.
[59] B. Liu, X. Ouyang, Y. Ding, L. Luo, D. Xu, Y. Ning, Electrochemical preparation of nickel and copper oxides-decorated graphene composite for simultaneous determination of dopamine, acetaminophen and tryptophan, Talanta 146 (2016) 114–121, https://doi.org/10.1016/j.talanta.2015.08.034.
[60] Q. Guo, T. Wu, L. Liu, H. Hou, S. Chen, L. Wang, Flexible and conductive titanium carbide-carbon nanofibers for the simultaneous determination of ascorbic acid, dopamine and uric acid, J. Mater. Chem. B 6 (2018) 4610–4617, https://doi.org/10.1039/c8tb00938d.
[61] D. Balram, K.Y. Lian, N. Sebastian, A novel electrochemical sensor based on flower shaped Zinc Oxide nanoparticles for the efficient detection of dopamine, Int. J. Electrochem. Sci. 13 (2018) 1542–1555, https://doi.org/10.20964/2018.02.06.
[62] N. Yılmaz Baran, Palladium nanoparticles decorated on a novel polyazomethine as a highly productive and recyclable catalyst for Suzuki coupling reactions and 4-nitrophenol reduction, J. Organomet. Chem. 899 (2019) 120886, , https://doi.org/

10.1016/j.jorganchem.2019.120886.
[63] L.Q. Xie, Y.H. Zhang, F. Gao, Q.A. Wu, P.Y. Xu, S.S. Wang, N.N. Gao, Q.X. Wang, A highly sensitive dopamine sensor based on a polyaniline/reduced graphene oxide/Nafion nanocomposite, Chin. Chem. Lett. 28 (2017) 41–48, https://doi.org/10.1016/j.cclet.2016.05.015.
[64] C. Zou, J. Zhong, S. Li, H. Wang, J. Wang, B. Yan, Y. Du, Fabrication of reduced graphene oxide-bimetallic PdAu nanocomposites for the electrochemical determination of ascorbic acid, dopamine, uric acid and rutin, J. Electroanal. Chem. 805 (2017) 110–119, https://doi.org/10.1016/j.jelechem.2017.10.020.